Detection of Localized Surface Uplift by Differential SAR Interferometry at the Hangingstone Oil Sand Field, Alberta, Canada

3 authors:

Mokhamad Yusup Nur Khakim
Universitas Sriwijaya
21 PUBLICATIONS   42 CITATIONS

Takeshi Tsuji
Kyushu University
296 PUBLICATIONS   2,169 CITATIONS

Toshi Matsuoka
Fukada Geological Institute
411 PUBLICATIONS   2,772 CITATIONS

Some of the authors of this publication are also working on these related projects:

Project Fossa Magna basin formation View project

Project Geophysical monitoring View project

Detection of Localized Surface Uplift by Differential SAR Interferometry at the Hangingstone Oil Sand Field, Alberta, Canada

Mokhamad Yusup Nur Khakim, Takeshi Tsuji, and Toshifumi Matsuoka

Abstract—We estimated the surface uplift (heave) rate due to steam-assisted gravity drainage (SAGD) at the Hangingstone oil sand field in Alberta, Canada, by stacking differential synthetic aperture radar (SAR) interferograms. To improve accuracy, a Landsat-7 Enhanced Thematic Mapper Plus intensity image was coregistered with the SAR intensity image. We examined three interferogram filtering methods and identified one that provided the desired effect of light filtering in areas of low noise and heavier filtering in high-noise areas. Based on our analysis of interferogram coherences, site-specific decorrelation highly depends on local seasonal changes. Stacking was performed to estimate the surface uplift rate while removing atmospheric and seasonal effects. The amounts of the uplift rate and slope change estimated by means of InSAR analysis reached a maximum of 3.6 cm/yr and 0.003%, respectively, for the period of 2007–2008. Comparison of the magnitude and patterns of the estimated surface uplift demonstrated that the uplift estimated from InSAR analysis agrees well with that obtained by conventional geodetic (GPS) surveys from a network of 54 monuments. Surface slope changes due to SAGD that we detected by using InSAR over one year in this oil sand field were small, so destruction of surface facilities by uplift is unlikely in the short term.

Index Terms—Adaptive filtering, interferogram stacking, steam injection, surface uplift.

I. INTRODUCTION

SUBSURFACE injection of fluids (i.e., water, gas, and vapor) can induce surface uplift. Although fluid injection has been used worldwide for many years and for a variety of purposes, for example, to mitigate anthropogenic land subsidence, recharge excessive abstraction from aquifer systems, and enhance oil recovery (EOR), surface uplift has been recognized less often than subsidence. Thermal EOR, such as steam-assisted gravity drainage (SAGD), used in oil sand reservoirs containing bitumen, can cause surface uplift in response to the increased pore pressure and temperature during injection [1]. In such cases, surface uplift may be relatively small, so it is not considered to be an environmental hazard and may not destroy engineering structures and other infrastructure in the short term. The amount of surface deformation can be used to estimate steam-chamber growth, knowledge of which is critical to optimize heavy oil recovery, to target the area of stimulation of the reservoir, and to identify bypass regions. For these reasons, there is an increasing demand for accurate monitoring of surface uplift. Deformation identified can be used to mitigate risks, to improve understanding of reservoir behavior and thus optimize oil production.

From 1999 to 2008, conventional geodetic (GPS) measurements from a network of 54 monuments were used to map surface uplift due to SAGD at the Hangingstone oil sand field [2]. The field is less than 50 km southwest of Fort McMurry, AB, Canada, and covers an area of approximately 16 km^2. GPS surveys provide a suitable conventional technique for measuring a 3-D deformation vector at each station with an accuracy of few millimeters. As an alternative and complimentary to precision ground survey of a network of survey monuments, synthetic aperture radar interferometry (InSAR) can be used to image ground surface deformations over large areas (several tens of square kilometers) and can identify small (1 cm or less) surface changes under all weather conditions day or night. It has proved to be a topographic mapping technique with high spatial resolution and accuracy [3]–[6] and is highly effective for monitoring deformation at the Earth's surface [7]–[14].

In this study, we investigated the ability of InSAR to accurately estimate small surface deformation at the Hangingstone oil sand field, a small area undergoing SAGD. We compared our results with those from conventional geodetic measurements using a network of 54 monuments [2]. Although InSAR is a powerful tool, it has limitations related to noise caused by decorrelation effects and water vapor in the atmosphere [15]. In geocoding, the accuracy of an initial geocoding lookup table is mainly limited by the accuracy of the available orbit geometry. By using automatic registration with the actual SAR intensity image, InSAR processing allows simulated SAR intensity images to be used to obtain positioning data at sub-pixel levels of accuracy. However, because of the low topographic relief of

M. Y. N. Khakim is with the Department of Physics, Mathematics and Natural Science Faculty, Sriwijaya University, South Sumatera, 30662, Indonesia (e-mail: myusup_nkh@yahoo.com).
T. Tsuji is with the International Institute for Carbon-Neutral Energy Research (WPI-I2CNER), Kyushu University, Kyushu 819-0395, Japan.
T. Matsuoka is with the Department of Urban Management, Kyoto University, Kyoto 615-8540, Japan.
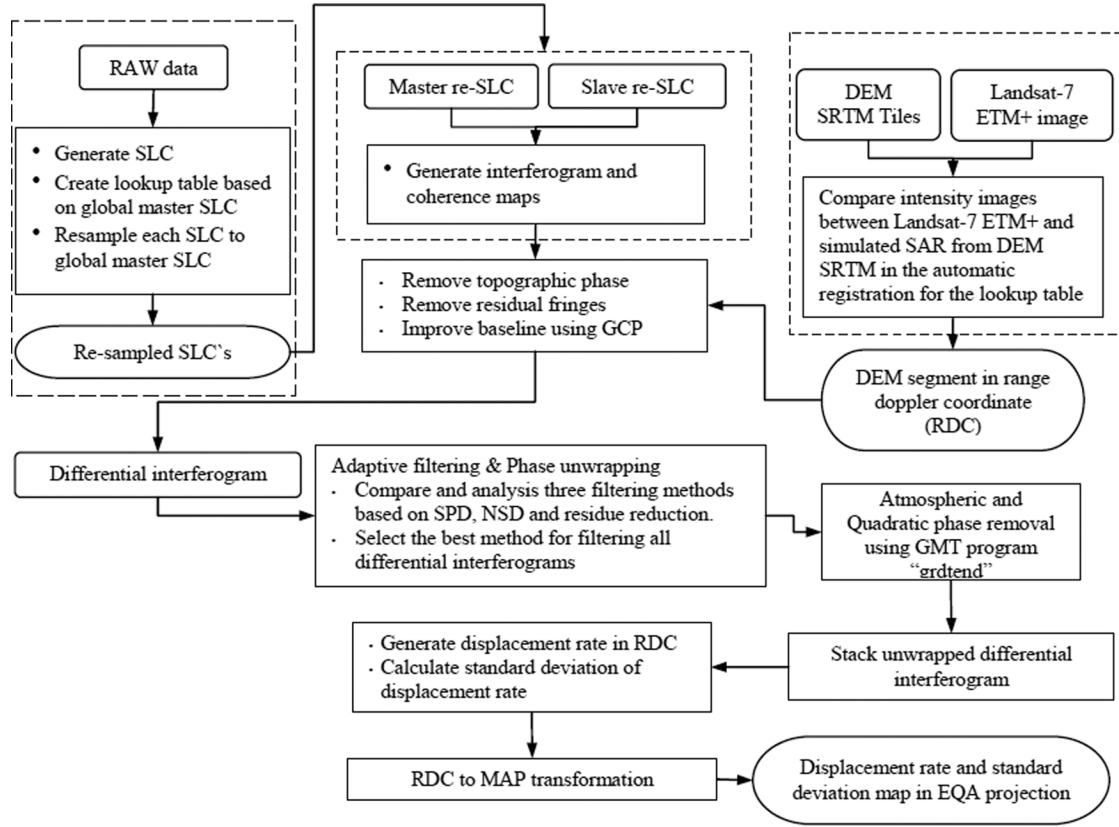
Fig. 1.   Processing flowchart for estimating surface deformation.

our study area, the simulated SAR intensity image generated from a digital elevation model obtained from Shuttle Radar Topography Mission (SRTM-DEM) data does not provide accuracy to subpixel level. This is a consequence of a strong decorrelation between the SAR intensity image from satellite measurements and the simulated SAR intensity image from SRTM-DEM. In this paper, we present a way to solve this problem so that refinement of the lookup table considerably improves accuracy.

The effect of atmospheric path delay can limit the accuracy of deformation estimated from differential InSAR (DInSAR). This effect is related to the presence of water vapor, which causes errors in estimations of displacement. Although this problem can be overcome by using persistent scatterer interferometry (PSI), this approach requires large PSI data stacks (e.g., more than 20 scenes). To overcome this problem, we reduced the atmospheric effect by stacking unwrapped differential SAR interferograms. Moreover, the main problem when processing InSAR data is the presence of residues in the phase unwrapping. These residues are caused by noise in interferograms. Goldstein and Werner [16], Baran *et al.* [17], and Li *et al.* [18] developed filtering methods to reduce noise. We compared the application of these filtering methods before unwrapping differential interferograms to allow us to choose the optimal method to reduce noise in differential interferograms. We also used other statistical parameters, such as the sum of the phase difference (SPD) and normalized standard deviation (NSD), to examine these filtering methods for application to interferograms from the Hangingstone oil sand field, which have relatively low coherence due

TABLE I
PALSAR DATA USED IN THIS STUDY

No.	Date acquired	Path/Row	Mode	Doppler centroid (Hz)
1.*	2007/02/09	194/112	FBS	68.6036
2.	2007/06/27	194/112	FBD	72.1220
3.	2007/08/12	194/112	FBD	81.7299
4.	2008/02/12	194/112	FBS	49.2399
5.	2008/05/14	194/112	FBD	70.2395
6.	2008/06/29	194/112	FBD	77.3937
7.	2008/09/29	194/112	FBD	70.1187

* Global master SLC used

to the swampy environment of the field. We used InSAR data acquired by the Phase Array type L-band (PALSAR) instrument on the Japanese Advanced Land Observation Satellite (ALOS) "Daichi". As the satellite was launched on 24 January, 2006, we investigated surface uplift from 2007 to 2008 [19].

II. METHODOLOGY

The main processing steps we employed to map surface deformation due to steam injection at the Hangingstone oil sand field were SAR processing, interferometric processing, geocoding, topographic phase removal, adaptive filtering, phase unwrapping, quadratic-phase removal, stacking, and conversion of the stacked unwrapped phase to vertical displacement rate (Fig. 1).

A. InSAR Data

We used seven images from PALSAR Level 1.0 data for the period from 9 February, 2007, to 29 September, 2008 (Table I).

This article has been accepted for inclusion in a future issue of this journal. Content is final as presented, with the exception of pagination.

KHAKIM *et al.*: DETECTION OF LOCALIZED SURFACE UPLIFT BY DIFFERENTIAL SAR INTERFEROMETRY 3
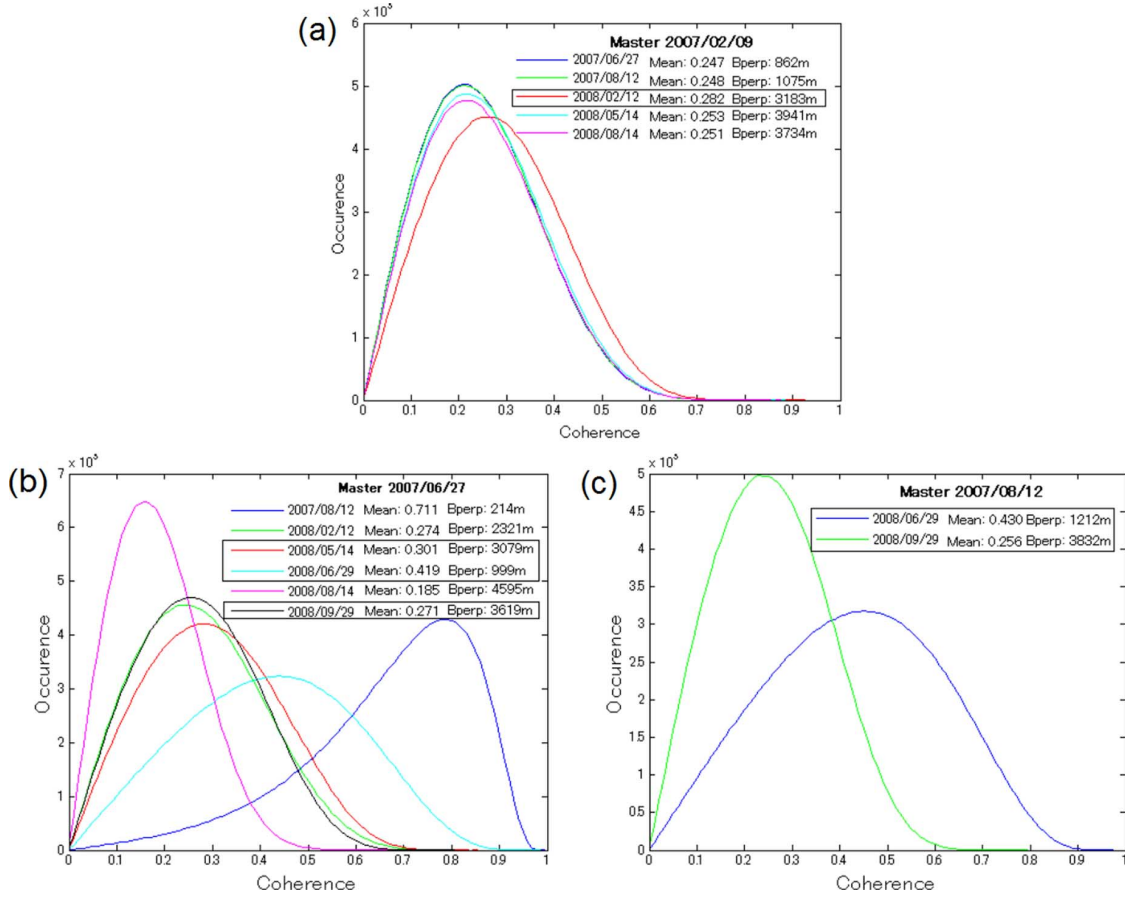

Fig. 2. Distributions of mean coherence of 13 interferograms with masters (a) 2007/02/09, (b) 2007/06/27, and (c) 2007/08/12. Rectangles around acquisition dates indicate good quality interferograms.

These data included fine-beam single polarization (FBS; HH polarization) and fine-beam double polarization (FBD; HH + HV polarizations) modes from ascending orbits with an off-nadir angle of 34.3°. The main advantages of L-band (23.6 cm wavelength) over C-band (5.6 cm wavelength) data are deeper penetration in vegetated areas, which results in less temporal decorrelation and enables a longer time separation between interferograms, and longer baselines, which provide more usable interferometric pairs.

B. Generation of Interferograms

Before producing interferograms, we generated seven single look complex (SLC) images from raw PALSAR data. To eliminate the effect of slightly different azimuths and imaging geometries, and to maintain coherence, all images were processed using a common Doppler centroid frequency of 69.15 Hz. A global master SLC (No. 1 in Table I) was selected and segmented around the area of the oil sand field undergoing SAGD. Segmentation reduces the time and amount of memory required for processing and provides clearer images of small target areas. All other SLC images were then coregistered to the global master SLC so that all had the same geometry. For interferogram generation, we applied a multilook approach with factors of 3 and 1 for azimuth and range directions, respectively.

To remove those parts of the image spectrum that did not contribute to the interferogram, we applied common-band filtering in both the range and azimuth directions [20]. These filters provide a type of phase coregistration, such that the contributions that are best correlated in the two images are retained. Both FBS and FBD modes were used for interferogram generation. A range that oversampled by a factor of two was applied to all FBD images to transform them to the same pixel spacing as the FBS images, thus allowing FBS/FBD coregistration [21]. After generation of interferograms, coherence (the complex correlation between the master and coregistered slave image) was calculated over a 5×5 pixel window for paired interferograms. This coherence provides a direct measure of the similarity of the dielectric properties of the pixels imaged by the two SAR datasets. We used coherence analysis to select appropriate interferogram pairs to map the rate of vertical displacement.

C. Geocoding

Because all images were coregistered to the global master image, we required only one lookup table for geocoding, for which we used SRTM-DEM data at 3 arcsec resolution. To cover the entire target area within the InSAR scene, we used a mosaic of six DEM tiles (N55W111, N55W112, N55W113, N56W111, N56W112, and N56W113). The dimensions of the resulting DEM were 3601 columns $\times$ 2401 lines and
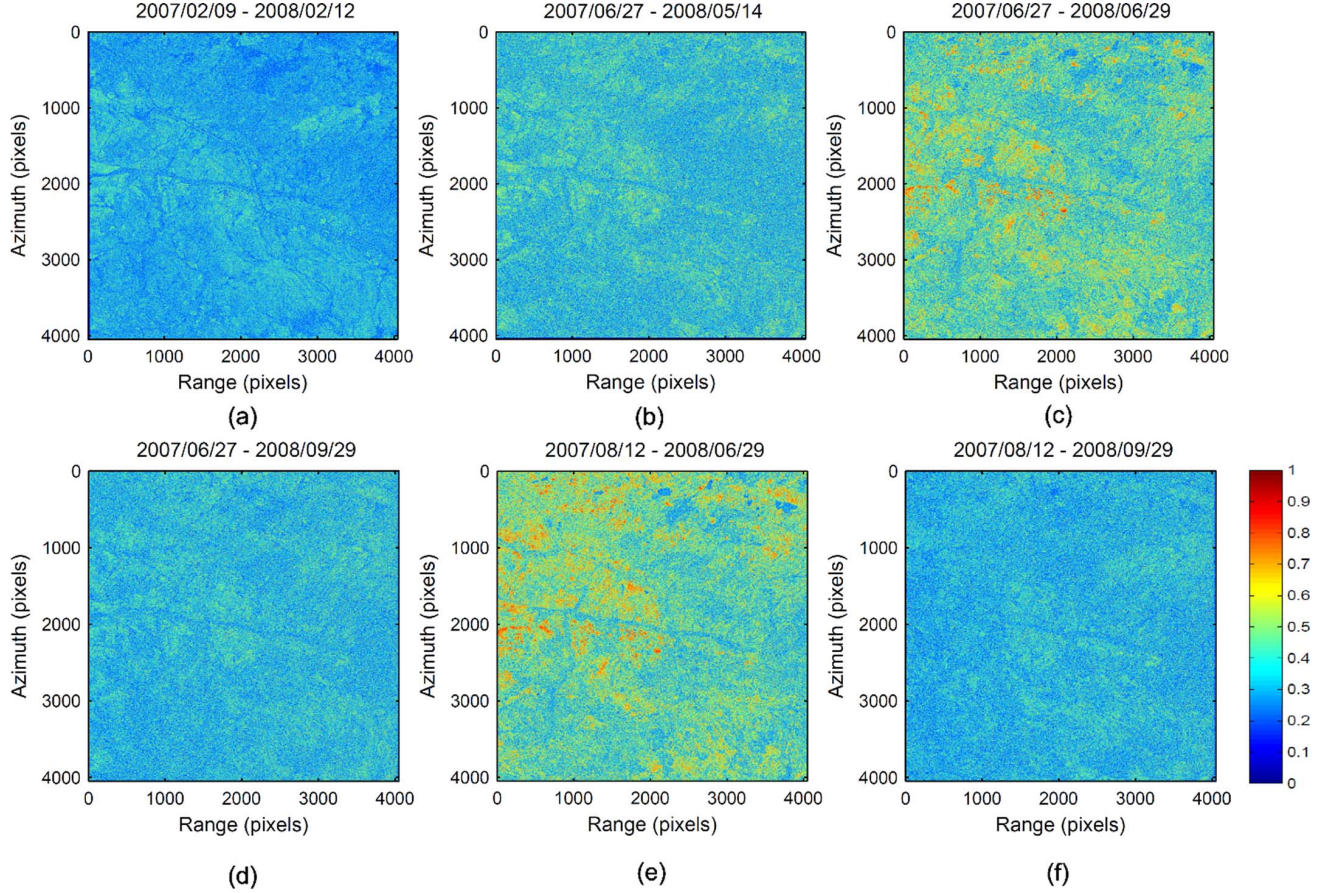
This article has been accepted for inclusion in a future issue of this journal. Content is final as presented, with the exception of pagination.

4

IEEE JOURNAL OF SELECTED TOPICS IN APPLIED EARTH OBSERVATIONS AND REMOTE SENSING

Fig. 3. Coherence maps for selected interferograms.

8.333333×10^{-4} decimal degrees for latitudinal and longitudinal pixel spacing using an equiangular (EQA) projection.

Coregistration of the actual SAR intensity image with the simulated SAR intensity image from SRTM-DEM is commonly required to refine the geocoding lookup table (LUT) to subpixel accuracy. We compared the benefits of using Landsat 7 Enhanced Thematic Mapper Plus ((ETM+) intensity images with those of using the simulated SAR intensity image derived from SRTM-DEM. Analyses of standard deviation, number of offset fit, and signal-to-noise ratio (SNR) threshold were used to estimate the sub-pixel accuracy of the coregistration process.

D. Adaptive Filtering for DInSAR Interferometry

'The aim of DInSAR is to separate topography from displacement-related phase terms, thus allowing retrieval and mapping of displacement. We used a two-pass differential interferometry approach in which the topography-related phase term was calculated from the DEM and transformed from EQA projection to a radar map. For this process, the topographic phase must be scaled according to the perpendicular baseline component. Therefore, precise knowledge of the baseline is important. The various estimations of baseline applied in this study were based on orbit data, the fringe rate of interferograms, and ground control points (GCPs). GCPs were selected on flat and highly correlated areas and they are spread over the entire image. We used a coherence map with the threshold value of 0.7 to extract the GCPs from DEM. The quality of selected GCPs determines the
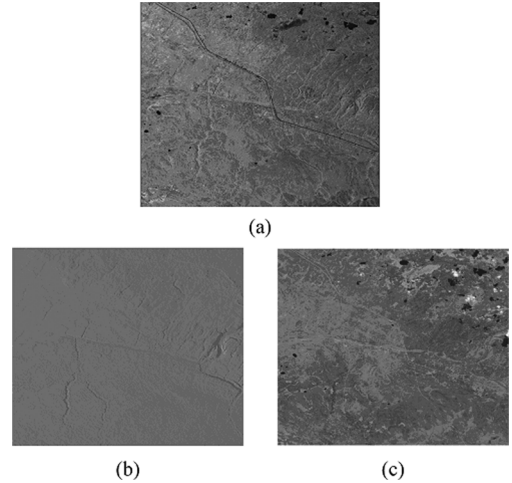

Fig. 4. Intensity image comparison. (a) PALSAR intensity. (b) Simulated SAR intensity from DEM. (c) Landsat ETM+ intensity.

accuracy of the baseline, thus resulting accurate InSAR-surface deformations.

After generation of the differential interferogram, adaptive filtering was applied to reduce phase noise. If phase noise is not properly removed from interferograms, it causes pseudo phase residues, which greatly affect phase unwrapping. We compared filtering techniques developed by Goldstein and Werner [16], Baran et al. [17], and Li et al. [18] (Goldstein, Baran, and Li

filters, respectively, hereafter) by applying each of them to one pair of differential interferograms and considering the resultant normalized standard deviations, sums of phase difference, and percentages of residue reduction. We also visualized the results of the three filtering methods to compare the smoothness of the filtered differential interferograms.

E. DInSAR Stacking

For large baseline changes along track due to squinted orbits, the differential interferogram still retains some residual phase components not yet compensated for after baseline corrections using GCPs and a baseline model. These residual phase components appear as linear or quadratic trends in the interferograms. To correct for such residual trends, we applied a detrending process by using the "grdtrend" component of the Generic Mapping Tools software package (GMT) [22]. This program locally fits phase variations to identify a trend and then removes it. This can be done using a three-parameter fit (a constant and coefficients of X and Y) for linear trend surfaces or a six-parameter fit (a constant and coefficients of X, Y, $X * Y$, X^2, and Y^2) for quadratic trend surfaces.

The accuracy of vertical displacements obtained from individual differential interferograms is limited mainly by the atmospheric path delay term. To reduce the effect of atmospheric disturbance, we used a stacking technique combining multiple observations into a single deformation map. The stacking was performed by taking a weighted average of interferograms with the time interval of interferogram as a weight [23]. The main assumption of the stacking technique is that the correlations of displacement phases between independent pairs of interferograms are strong and are therefore enhanced by stacking, whereas the error terms such as atmospheric effects, signal noise, and other decorrelations are random and are therefore suppressed by stacking [24]. Because the amount of displacement between interferometric pairs increases with acquisition interval, pairs separated by long intervals will better reduce the relative effect of atmospheric disturbances. Furthermore, because atmospheric errors are independent of the interval between interferograms, pairs separated by shorter intervals will have greater errors in estimates of small uplift. Therefore, to map displacements we preferentially selected interferograms at acquisition intervals of about one year or more.

III. RESULTS AND DISCUSSION

A. Coherence in Area of Interest

The most important aspect of the estimation of displacement rate by using a stacking method is the selection of the interferograms to be combined. The quality of an interferogram can be measured in terms of its coherency. From seven ALOS datasets, we generated 13 interferograms over the study area and analyzed their coherence. Fig. 2 illustrates the mean coherence of these interferograms with different master images. Most of the interferograms over the area of interest show low coherence due either to temporal decorrelation or to their long perpendicular
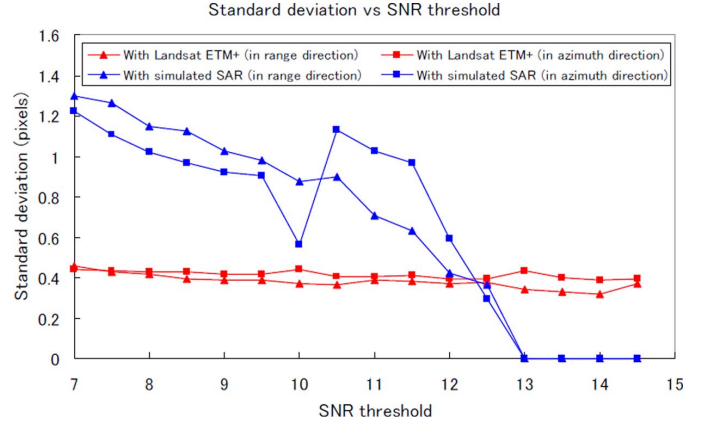

Fig. 5. Standard deviation as a function of SNR threshold with simulated SAR intensity (blue color) and with Landsat ETM+ (red color).
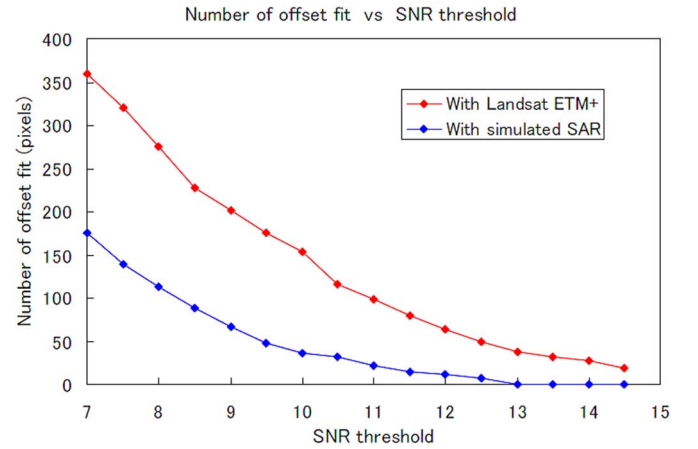

Fig. 6. Number of offset fit as function of SNR threshold with simulated SAR intensity (blue color) and with Landsat ETM+ (red color).

baselines (around 3000 m). The coherence values are less than 0.3, which indicates vegetated or irrigated farmland areas [25]. Only a few interferogram pairs have short perpendicular baselines (less than 1000 m).

It is noteworthy that the intervals between pairs of SAR acquisitions and the perpendicular baseline lengths of the first two pairs using master scene 2007/02/09 are shorter than other pairs; their coherences are not as good as expected. In general, the interferograms generated with master scene 2007/02/09 have comparatively low coherence, indicating that decorrelation is most severe in winter (February 2007). This may be a reflection of heavy snow cover in the area of interest and its surroundings. However, the interferometric pair 2007/02/09–2008/02/12, which are separated by a longer time interval and have a longer perpendicular baseline than the aforementioned pairs, have a higher coherence (0.28). It is to be expected that the dielectric properties of pixels representing the same location but imaged from different SAR acquisitions in the same season would have high similarity. Interferograms generated from two acquisitions in the same season and showing high coherence are evident in other pairs, such as the 06/27/

This article has been accepted for inclusion in a future issue of this journal. Content is final as presented, with the exception of pagination.

6

IEEE JOURNAL OF SELECTED TOPICS IN APPLIED EARTH OBSERVATIONS AND REMOTE SENSING
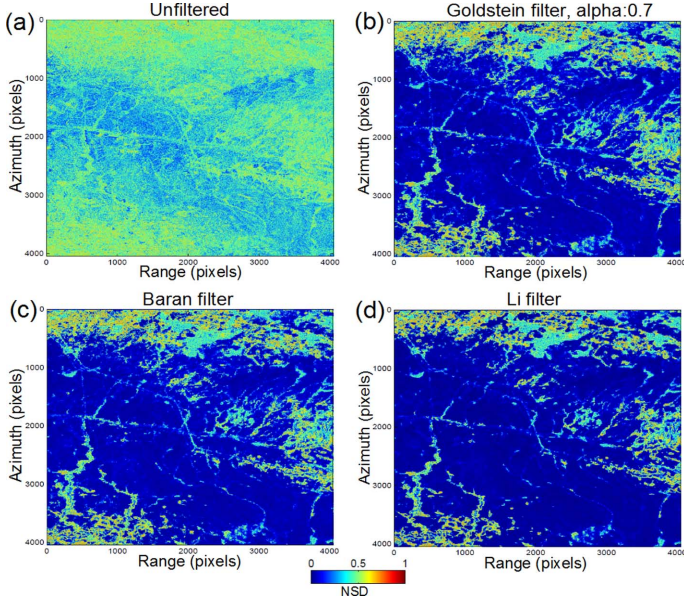
Fig. 7. NSD of a differential interferogram. (a) Unfiltered. Filtered with (b) Goldstein filter ($\alpha = 0.7$), (c) Baran filter, and (d) Li filter.

TABLE II
EVALUATION OF FILTER PERFORMANCE: RESIDUE REDUCTION AND SPD

Filter	Number of residues		Residue reduction (%)	SPD (radians)
	Negative	Positive		
Unfiltered	2560492	2560621	-	3.2965e+007
Goldstein ($\alpha = 0.7$)	258248	258267	90	1.2466e+007
Baran	226926	226942	91	1.1903e+007
Li	150518	149531	94	8.7456e+006

2007–06/29/2008 pairing. Thus, good interferograms were generated in our study area when derived from two acquisitions in the same season.

For the identification of small surface displacements, interferograms obtained by pairing data separated by longer time intervals should provide better signal-to-atmospheric-noise ratios, as long as they also have good coherence. Because such pairings suffer from greater decorrelation, we selected interferogram pairs with temporal baselines of about one year. From our coherence analysis, selected interferograms of reasonably good quality are indicated in Fig. 2(a)–(c) by rectangles placed around their acquisition dates. Fig. 3 shows coherence maps of selected interferograms used to estimate the uplift rate due to SAGD. Overall, coherence in the area of interest is high; the lowest values are related to rivers and ponds, which are clearly evident in Fig. 3. Mean coherence values are between 0.26 and 0.42. The quality of the interferograms can be improved by using adaptive filtering to reduce noise, thus increasing coherence. Our investigation of different adaptive filtering methods is discussed in Section III-C.

B. Refinement of LUT Using Landsat ETM+ Image in Geocoding

Simulated SAR intensity is proportional to local incidence angle according to the surface backscattering phase function [26]. Therefore, poor estimation of the offset between PALSAR
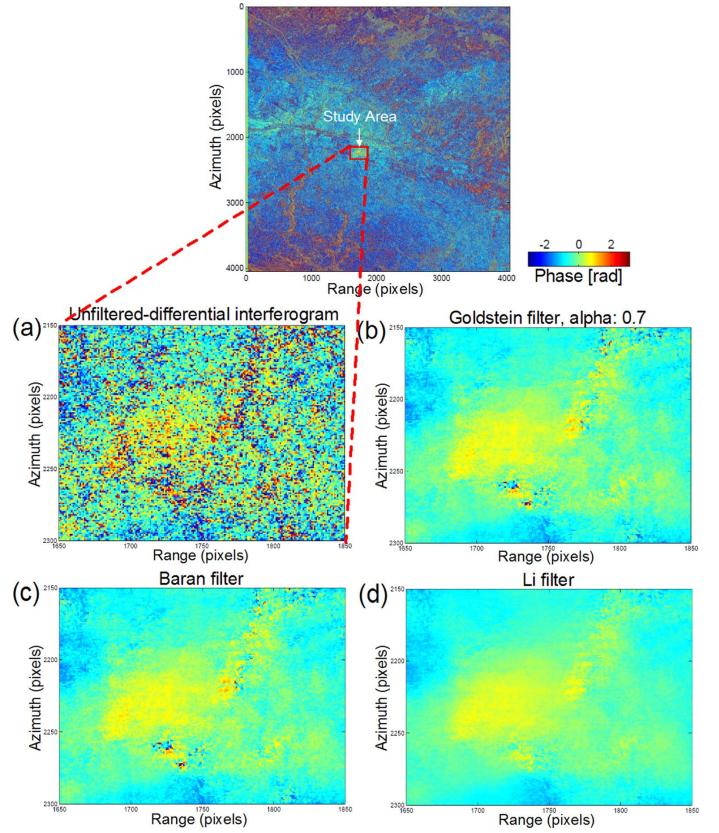

Fig. 8. Differential interferograms. (a) Unfiltered interferogram. Filtered interferograms with (b) Goldstein filter ($\alpha = 0.7$), (c) Baran filter, and (d) Li filter.

intensity and the simulated SAR intensity is evident in part of our study area because of its moderate topography. The PALSAR image shows many features that can also be observed in the Landsat ETM+ image. Therefore, the automatic registration procedure using the Landsat ETM+ image instead of the simulated SAR image provides greater accuracy. Comparisons of the PALSAR, the Landsat ETM+, and the simulated SAR images are shown in Fig. 4.

Comparison of standard deviations with SNR thresholds for coregistration with Landsat intensity and with simulated SAR intensity (Fig. 5) shows that the standard deviations of the former are lower than those of the latter. When coregistered with Landsat intensity, the standard deviation is less than 0.5 pixel; thus sub-pixel accuracy is achieved. Coregistration with the simulated SAR intensity reduces accuracy to greater than one pixel. Furthermore, the numbers of fit offsets for coregistration with Landsat intensity are higher than those obtained for co-registration with the simulated SAR intensity (Fig. 6). Therefore, for refinement of the LUT, coregistration with the Landsat intensity provides much greater accuracy than coregistration with the simulated SAR intensity.

C. Comparison of the Goldstein, Baran, and Li Adaptive Filtering Methods

For the comparison of the three filtering methods, we used the interferometric pair 2007/02/09–2008/02/12. Coherence, a measure of phase noise, is defined as the magnitude of the normalized interferogram. To measure coherence quantitatively,

This article has been accepted for inclusion in a future issue of this journal. Content is final as presented, with the exception of pagination.

KHAKIM *et al.*: DETECTION OF LOCALIZED SURFACE UPLIFT BY DIFFERENTIAL SAR INTERFEROMETRY
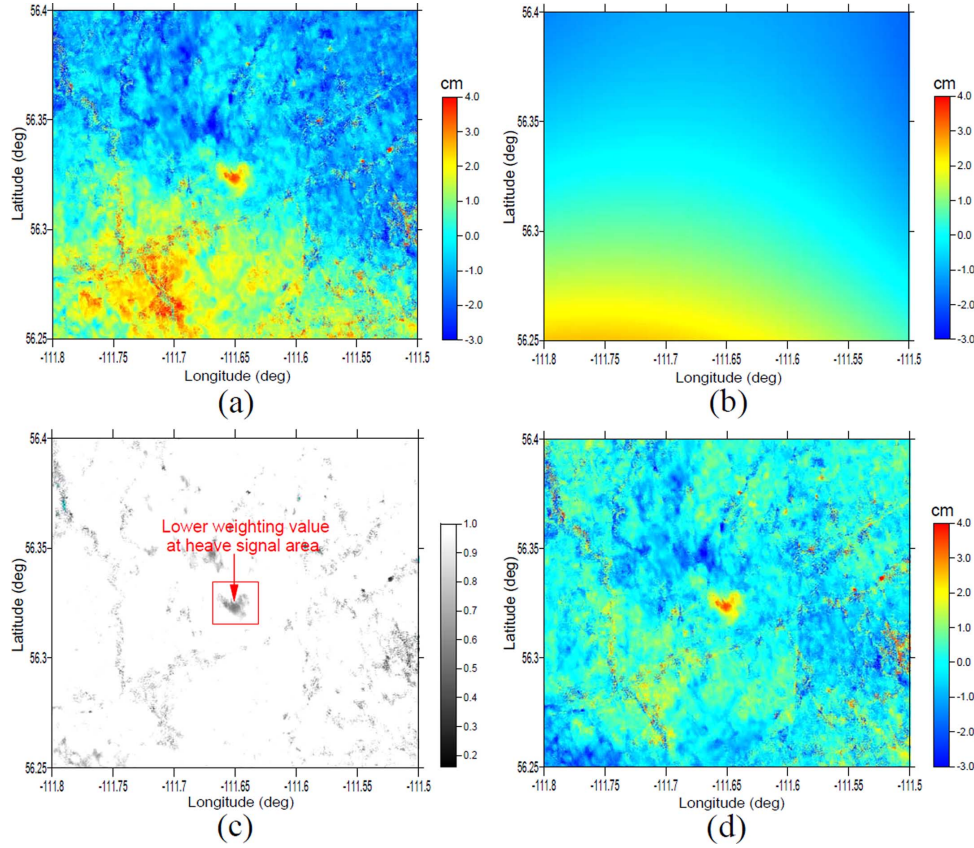
7

Fig. 9. Quadratic trend removal. (a) Before detrending. (b) Quadratic trend. (c) Weighting map. (d) Detrended uplift.

we created distributions of image coherence as discussed in Section III-A. The Goldstein filter uses a filtering constant α for all parts of an interferogram, which is determined from a noise-level interferogram. Based on the coherence, we therefore used $\alpha = 0.7$ to make the Goldstein filter comparable with the Baran filter. For the three filters considered here (Goldstein, Baran, and Li), we used a patch size of 32×32 pixels and window overlap of 14 pixels. For the Goldstein and Baran filters, we employed a smoothing operator with a mean kernel of 3×3 pixels.

The first criterion we used to evaluate the effectiveness of the filters was the normalized standard deviation (NSD), which quantifies the general noise level of an interferogram. Comparison of NSD for interferograms after filtering by the three methods [Fig. 7] shows very high NSD (about 0.5 or more) for the unfiltered interferogram [Fig. 7(a)]. The Goldstein and Baran filters provided a considerable and similar reduction of noise level [Fig. 7(b) and (c)]. This similarity of noise reduction reflects the similarity of the exponents of the filtering parameters of both methods. Differences among the filtered NSD images can be clearly seen in the upper, lower, and right-hand parts of the images. However, based on NSD for the data from our study area, the Li filter provided the most effective reduction of noise [Fig. 7(d)], as indicated by the greater area of low SND (blue in Fig. 7).

Other, more reliable, criteria for analysis of filter effectiveness are SPD and residue reduction (Table II). The reductions in the number of residues after application of the Li, Baran,

and Goldstein filters were 94%, 91%, and 90%, respectively. The percentage SPD improvements of the interferograms for Li, Baran, and Goldstein filters were 74%, 64%, and 62%, respectively. These results confirm that the Li filter is the most effective method to minimize SPD and to maximize residue reduction.

Comparison of differential interferograms after filtering by the three methods (Fig. 8), focusing on the central part of the interferogram where a SAGD project is in operation, clearly shows the effect of filtering over the area deformed by steam injection. The unfiltered interferogram is contaminated by strong noise, which is substantially reduced by application of each of the three filters [Fig. 8(c)–(e)]. Noise reduction achieved by the Li filter was greater than that of the Baran filter, which was greater than that of the Goldstein filter. Application of the Li filter has effectively removed the noise and greatly improved the interferogram. For a small area such as the part of our study area affected by SAGD, with small deformation and strong noise, our results show that the Li filter is the most suitable method of noise reduction to use before phase unwrapping.

D. Estimation of Surface Uplift Rate and Slope Change

Systematic fringe patterns due to baseline inaccuracy were successfully reduced by using fringe rates, GCPs, and baseline models, as mentioned in Section II-D. A residual phase trend due to squinted orbits was then effectively removed by using the "grdtrend" trend-fitting program of the GMT software package
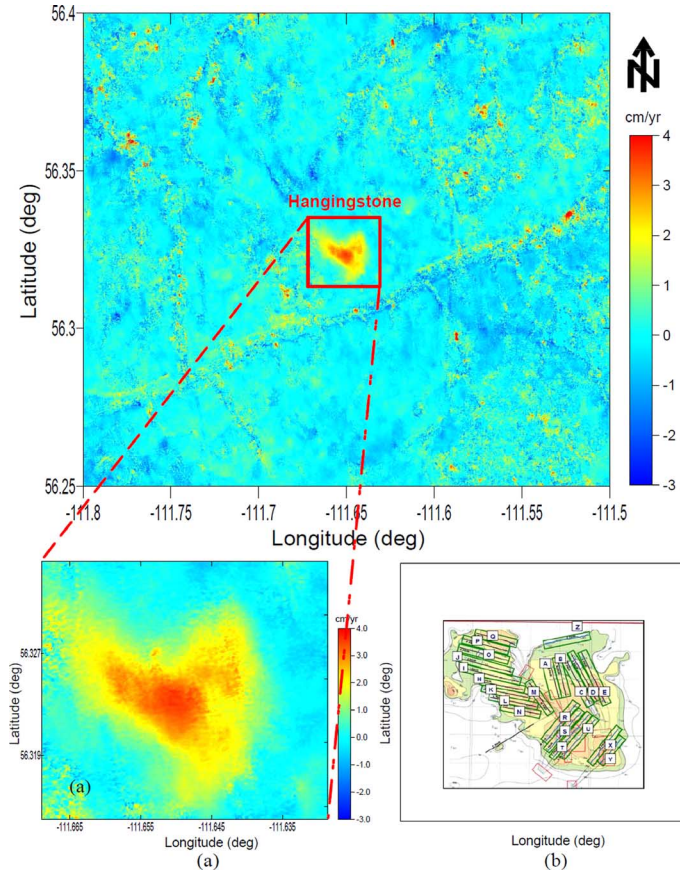
Fig. 10. (a) Map of vertical displacement rate derived from stacking of unwrapped differential interferograms. (b) Distribution of injection wells [2].

[22]. This program iteratively processes fitting data, locates outliers, calculates a weighting map, and then fits the data again using the calculated weights. An interferogram after conversion to vertical displacement clearly shows the presence of a phase trend [Fig. 9(a)]. For this case, we applied quadratic detrending with a six-parameter fit. The estimated quadratic trend from this interferogram is shown in Fig. 9(b). The fitting process detected the uplift signal at the Hangingstone oil sand field and then automatically lowered the weights in that region [Fig. 9(c)]. Therefore, because the signal we wanted to measure did not affect the trend surface fit, the vertical displacement after detrending was much improved [Fig. 9(d)].

For surface uplift measurements over a small area such as that at Hangingstone, the most important errors are derived from white noise and atmospheric effects. White noise, presented as random phases over short distances in our interferograms because of spatial and temporal decorrelation, was reduced. For such cases, a multi-looking operation in azimuth and range direction can be applied. In addition, the Li filter effectively smoothed the interferograms, as described in Section III-C. However, the temporal decorrelation changes in the ground surface between two SAR images (e.g., the effect of trees, bushes, snow, and surface facilities of oil field) commonly affect interferograms.

Based on our coherence analysis, we generated six independent differential interferograms to estimate the vertical displace-

ment rate by applying a stacking technique. The vertical displacement rate was calculated over the part of the oil sand field undergoing steam injection from 2007 to 2008. We assumed that the displacement over this area was linear over that period. After quadratic phase removal from the unwrapped differential interferograms, we stacked six interferograms to produce a deformation map. The magnitude of the displacements is positive over the area where SAGD injection/production well pairs were in operation. The positive displacements indicate ground surface uplift due to geomechanical phenomena associated with the SAGD process. The InSAR-generated map of uplift in the Hangingstone oil sand field delineates a main feature, an uplift pattern elongated in the northwest-southeast direction with a maximum uplift rate of around 3.6 cm/yr [Fig. 10(a)]. Since well pairs are placed in parallel and closed each other, injection pressure from each wellpair, which has contribution in deformation at each surface point, cumulatively caused a peak of the uplift around the center of well pair layout. The distribution of uplift corresponds well with the layout of the well pairs [Fig. 10(b)]. Variations of the amount of uplift may reflect different starting times of injection for individual wells.

To validate our results, we compared InSAR-derived uplift estimations with those derived from the network of 54 geodetic survey points [2]. The amount of uplift estimated by geodetic survey for periods of 1999–2008 [Fig. 11(a)] and 2007–2008 [Fig. 11(b)] reaches maximum of 23.9 cm and 3.9 cm, respectively. The contour patterns of vertical displacement from InSAR analysis [Fig. 11(c)] agree well with those from the geodetic survey data [Fig. 11(a) and (b)]. These results confirm that the interferogram stacking technique we used has accurately estimated the rate of surface displacement due to SAGD at the Hangingstone oil sand field.

The five yellow lines (O-A to O-E) shown in Fig. 11(b) indicate the transects along which we estimated slope changes caused by uplift to characterize the uplift slope. The maximum annual change of slope was calculated to be 0.003% (3×10^{-5} degrees) for lines O-B, O-C, and O-E. The changes of slope along lines O-D and O-A were 0.001% and 0.002%, respectively. Since the slope estimated from the network survey of 54 geodetic monuments was only along a red line F-G in Fig. 11(a) with a maximum of 0.043% from 1999 to 2008 [2], we used only one slope [line F-G in Fig. 11(b)] to quantitatively validate the uplift slope obtained from InSAR [Fig. 11(c)]. The estimated slope changes during SAGD process from 2007 to 2008 were 0.00086% and 0.00076% obtained from the geodetic and InSAR techniques, respectively. The slope change obtained from InSAR is relatively less smaller than that from geodetic technique. This difference may due to the decorrelation and atmospheric effects presenting in InSAR data. Annual changes of slope of this magnitude reflect uplift that is unlikely to destroy surface facilities within a single year. Structural design tolerances for surface facilities at Hangingstone were based on a maximum uplift of 40 cm and a maximum slope change of 0.12% for ten years [2].

An interesting characteristic of the surface uplift at this study area is that the position of uplift peak obtained from geodetic technique for the period of 1999–2008 [Fig. 11(a)] is in the northeast side of those from both geodetic and InSAR tech-

This article has been accepted for inclusion in a future issue of this journal. Content is final as presented, with the exception of pagination.

KHAKIM *et al.*: DETECTION OF LOCALIZED SURFACE UPLIFT BY DIFFERENTIAL SAR INTERFEROMETRY
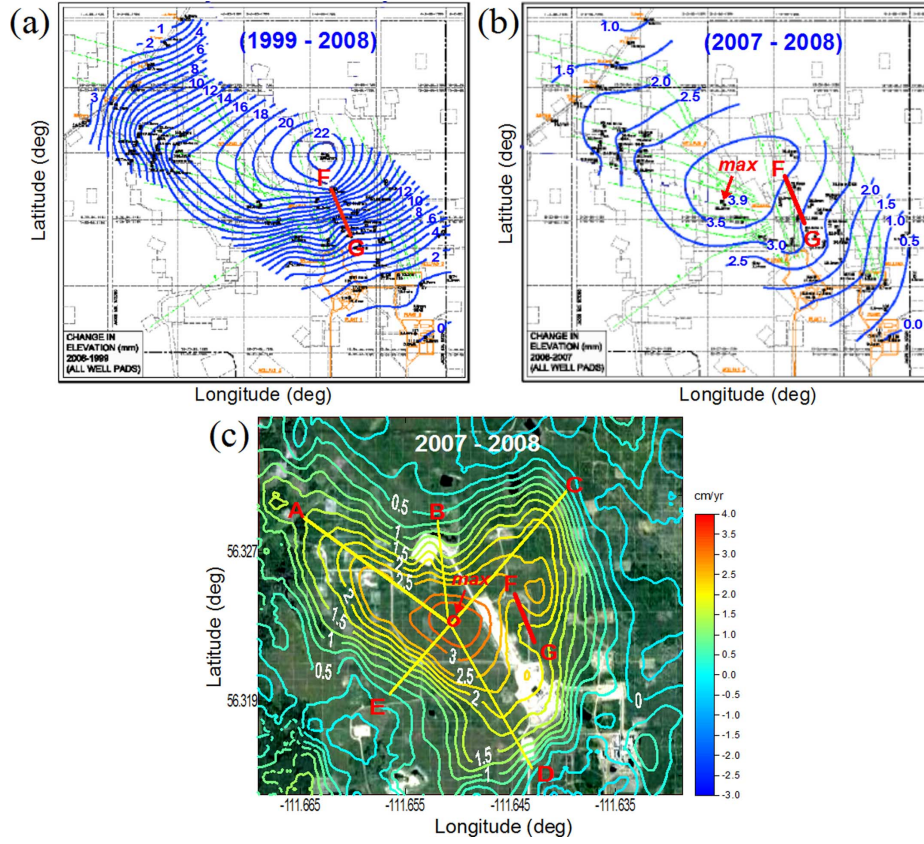
9

Fig. 11. Contours of surface uplift estimated from (a), (b) conventional geodetic surveys for periods of 1999–2008 and 2007–2008, respectively [2], and (c) InSAR analysis for a period of 2007–2008.
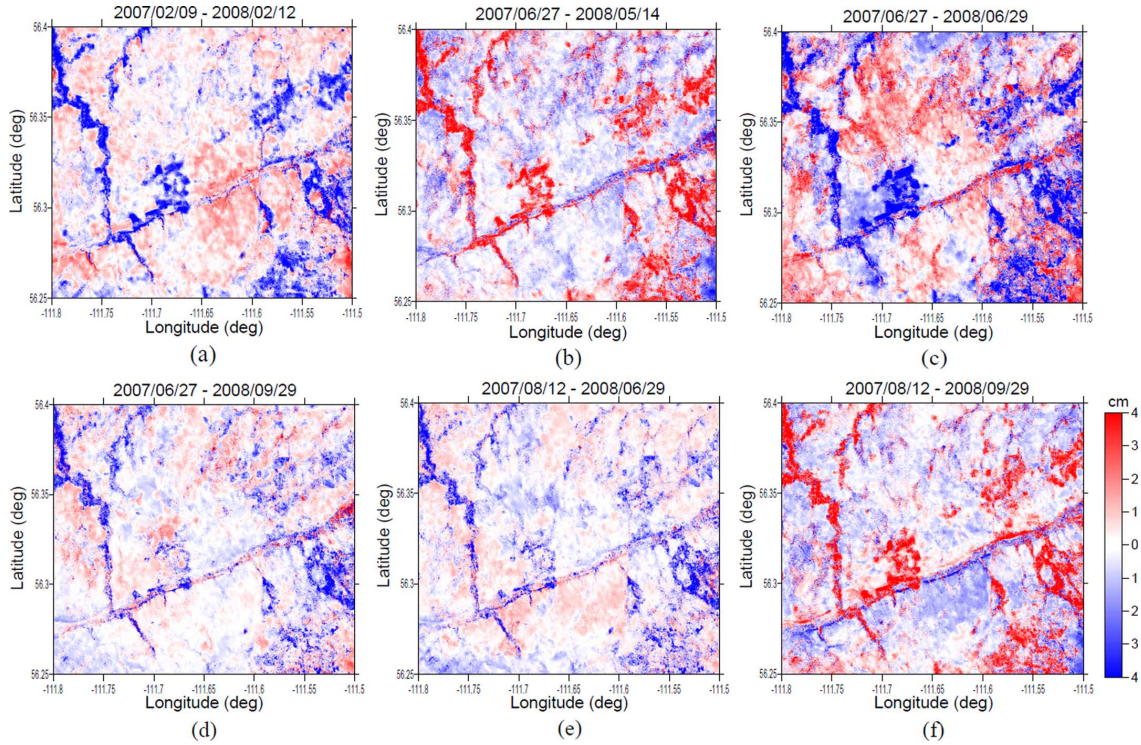

Fig. 12. Selected interferograms illustrating atmospheric effects, decorrelation errors, and seasonal effects.

niques for the period of 2007–2008 [Fig. 11(b) and (c)]. It indicates that the steam injection from injection wells in the north-

west and southeast parts of study area has larger effects in uplift developments than those in the northeast part for the period of

This article has been accepted for inclusion in a future issue of this journal. Content is final as presented, with the exception of pagination.

10   IEEE JOURNAL OF SELECTED TOPICS IN APPLIED EARTH OBSERVATIONS AND REMOTE SENSING

2007–2008. But the injection from injection wells in the north-east part has large effects in the cumulative uplift development for the period of 1999–2008.

To visualize the effectiveness of the stacking technique in removing the effects of atmospheric changes and decorrelation, we generated error maps by subtracting the uplift rates we calculated by the stacking technique from individual uplift maps with overlapping time intervals (Fig. 12). These maps clearly show errors due to both seasonal variations of SAR acquisition and temporal decorrelation. The errors have similar patterns, but opposite values, so stacking removed them effectively and provided us with accurate uplift rates.

IV. CONCLUSION

We presented a method of processing InSAR data to reveal small-scale surface displacements at the Hangingstone oil sand field SAGD site. In particular, we used Landsat ETM+ intensity data to refine lookup tables and determined which of three available adaptive filtering methods provided the optimum results. Our main findings are described below.

(1) Refinement of LUTs by coregistration of PALSAR intensity data with Landsat ETM+ intensity data provided greater accuracy than coregistration with simulated SAR intensity. Accuracy to less than a half pixel was achieved using the Landsat image, thus allowing better topographic phase removal from interferograms.

(2) Evaluation and comparison of Goldstein, Baran, and Li adaptive filtering methods showed that the Li filter provided the most effective reduction of noise in differential interferograms, especially for strong noise due to decorrelation effects.

The estimates of surface displacement we obtained from our InSAR analysis indicated a surface uplift rate of 3.6 cm/yr related to steam injection at the Hangingstone oil sand field and the distribution of uplift we obtained agreed well with that obtained by the conventional geodetic surveys from the network of 54 monuments.

The InSAR technique can successfully estimate uplift over study area, but the surface geodetic survey can accurately estimate the uplift only in area existing the network of geodetic monuments. An unavailability of the data file of ground geodetic surveys limits our InSAR results to be more quantitatively validated. However, the pattern, contours, and level of surface uplift from our results generally agree well with those of the network surveys.

In order to extend this study, we will apply this methodology, which uses the Landsat ETM+ data and Li filter, to interferometric point target analysis in future work.

REFERENCES

[1] P. M. Collins, "Geomechanical effects on the SAGD process," in *Proc. Int. Thermal Operations and Heavy Oil Symp.*, Calgary, AB, Canada, Nov. 1–3, 2005, SPE/PS-CIM/CHOA/PS2005-97905.

[2] Hangingstone Demonstration Project Japan Canada Oil Sands Ltd., Thermal In Situ Scheme Progress Rep., Approval No. 8788G, 2009.

[3] L. Graham, "Synthesis interferometric radar for topographic mapping," *Proc. IEEE*, vol. 62, pp. 763–768, 1974.

[4] S. N. Madsen, H. A. Zebker, and J. Martin, "Topographic mapping using radar interferometry: Processing techniques," *IEEE Trans. Geosci. Remote Sens.*, vol. 31, no. 1, pp. 246–256, Jan. 1993.

[5] H. A. Zebker, C. L. Werner, P. A. Rosen, and S. Hensley, "Accuracy of topographic maps derived from ERS-1 interferometric radar," *IEEE Trans. Geosci. Remote Sens.*, vol. 32, no. 4, pp. 823–836, Jul. 1994.

[6] E. Sansosti, R. Lanari, G. Fornaro, G. Fransceschetti, M. Tesauro, G. Puglisi, and M. Coltelli, "Digital elevation model generation using ascending and descending ERS-1/ERS-2 tandem data," *Int. J. Remote Sensing*, vol. 20, pp. 1527–1547, 1999.

[7] A. G. Gabriel, R. M. Goldstein, and H. A. Zebker, "Mapping small elevation changes over large areas: Differential radar interferometry," *J. Geophys. Res.*, vol. 94, pp. 9183–9191, 1989.

[8] D. Massonet, M. Rossi, C. Carmona, F. Adragna, G. Peltzer, K. L. Feigl, and T. Rabaute, "The displacement field of the Landers earthquake mapped by radar interferometry," *Nature*, vol. 364, pp. 138–142, 1993.

[9] G. Peltzer and P. Rosen, "Surface displacement of the 17 May 1993 Eureka Valley, California, earthquake observed by SAR interferometry," *Sci.*, vol. 268, pp. 1333–1336, 1995.

[10] X. L. Ding, G. X. Liu, Z. W. Li, Z. L. Li, and Y. Q. Chen, "Ground subsidence monitoring in Hong Kong with satellite SAR interferometry," *Photogrammetric Eng. Remote Sensing*, vol. 70, pp. 1151–1156, 2004.

[11] P. López-Quiroz, M. P. Doin, F. Tupin, P. Briole, and J. M. Nicolas, "Time series analysis of Mexico City subsidence constrained by radar interferometry," *J. Appl. Geophys.*, vol. 69, pp. 1–15, 2009.

[12] E. Papageorgiou, M. Foumelis, and I. Parcharidis, "Long-and short-term deformation monitoring of Santorini volcano: Unrest evidence by DInSAR analysis," *IEEE J. Sel. Topics Appl. Earth Observ.*, vol. 5, no. 5, pp. 1531–1537, 2012.

[13] L. Tao, H. Zhang, C. Y. Wang, and X. Tang, "Ground deformation retrieval using quasi coherent targets DInSAR, with application to suburban area of Tianjin, China," *IEEE J. Sel. Topics Appl. Earth Observ.*, vol. 5, no. 3, pp. 867–873, 2012.

[14] T. Tsuji, K. Yamamoto, T. Matsuoka, Y. Yamada, K. Onishi, A. Bahar, I. Meilano, and H. Z. Abidin, "Earthquake fault of the 26 May 2006 Yogyakarta earthquake observed by SAR interferometry," *Earth Planets Space (E-Lett.)*, vol. 61, pp. e29–e32, 2009.

[15] H. A. Zebker and J. Villasenor, "Decorrelation in interferometric radar echoes," *IEEE Trans. Geosci. Remote Sens.*, vol. 30, no. 5, pp. 950–959, Nov. 1992.

[16] R. M. Goldstein and C. L. Werner, "Radar interferogram filtering for geophysical applications," *Geophys. Res. Lett.*, vol. 25, pp. 4035–4038, 1998.

[17] I. Baran, M. P. Steward, B. M. Kampes, Z. Perski, and P. A. Lilly, "Modification to the Goldstein radar interferogram filter," *IEEE Trans. Geosci. Remote Sens.*, vol. 41, no. 4, pp. 950–959, Apr. 2003.

[18] Z. W. Li, X. L. Ding, C. Huang, D. W. Zheng, W. B. Zou, and Y. K. Shea, "Filtering method for SAR interferograms with strong noise," *Int. J. Remote Sens.*, vol. 27, pp. 2991–3000, 2006.

[19] *"PALSAR User's Guide,"* 1st ed. ERSDAC, 2006.

[20] A. Ferretti, A. Monti-Guarnieri, C. Prati, and F. Rocca, "InSAR Principles: Guidelines for SAR interferometry processing and Interpretation," *ESA*, 2007.

[21] C. Werner, U. Wegmüller, T. Strozzi, A. Wiesmann, and M. Santoro, "PALSAR multi-mode interferometric processing," in *Proc. First Joint PI Symp. ALOS Data Nodes for ALOS Sci. Program*, Kyoto, Japan, Nov. 19–23, 2007, pp. 19–23.

[22] P. Wessel and W. H. F. Smith, "Free software helps map and display data," *Eos, Trans., Amer. Geophysical Union*, vol. 72, pp. 441–448.

[23] D. T. Sandwell and E. J. Price, "Phase gradient approach to stacking interferogram," *J. Geophys. Res.*, vol. 103, no. B12, pp. 30183–30204, 1998.

[24] R. F. Hanssen, *Radar Interferometry: Data Interpretation and Error Analysis*. Dordrecht, The Netherlands: Kluwer Academic, 2001, vol. 2.

[25] M. Wei and D. T. Sandwell, "Decorrelation of L-band and C-band interferometry over vegetated areas in California," *IEEE Trans. Geosci. Remote Sens.*, vol. 48, no. 7, pp. 2942–2952, Jul. 2010.

[26] P. A. Rosen, S. Hensley, H. A. Zebker, and F. H. Webb, "Surface deformation and coherence measurement of Kilauea Volcano, Hawaii, from SIR-C radar interferometry," *J. Geophys. Res.*, vol. 101, pp. 109–125, 1996.

Takeshi Tsuji received the B.S. degree in resources engineering from Waseda University, Waseda, Japan, in 2002, and the M.Sc. degree and Ph.D. degree in earth and planetary science from the University of Tokyo, Tokyo, Japan, in 2004 and 2007, respectively.

Since 2007, he was an Assistant Professor of the Engineering Geology Group with Kyoto University, Kyoto, Japan. From 2010 to 2011, he was with Stanford University, Stanford, CA, USA. Since 2012, he has been an Associate Professor with the International Institute for Carbon-Neutral Energy Research (WPI-I2CNER), Kyushu University, Kyushu, Japan. His research interests include seismic reflection and refraction analysis, surface wave analysis, seismic attributes analysis, rock physics, seismic anisotropy, seismic interferometry, and interferometric SAR.

Mokhamad Yusup Nur Khakim received the B.Sc. degree in physics from Brawijaya University, Malang, Indonesia, in 1997, the M.Sc. degree in geophysics from Gadjah Mada University, Yogyakarta, Indonesia, in 2001, and the Ph.D. degree in civil and earth resources engineering from Kyoto University, Kyoto, Japan, in 2012.

He is currently a Lecturer with Sriwijaya University, Indonesia. His main research interests are SAR interferometry for natural disaster and reservoir monitoring, geomechanical modeling, and 4-D seismic and seismic refraction analysis.

Dr. Khakim is a member of AGU, SEG Japan, and the Indonesian Association of Geophysicist.

Toshifumi Matsuoka received the B.Sc. and M.Sc. degrees in physics from Tokyo University of Science, Tokyo, Japan, in 1973 and 1975, respectively, and the Ph.D. degree from the University of Tokyo, Tokyo, Japan, in 1995.

He joined Japan Petroleum Exploration Co., Ltd. in 1975 as a Research Geophysicist. From 1983 to 1985, he was with the University of British Colombia. In 1998, he joined Kyoto University, Kyoto, Japan, where he is currently a Professor with the Engineering Geology Group. He has over 30 years of experience as researcher, manager of research projects, and educator. He has been working seismic exploration, time series analysis, and remote sensing areas.

Dr. Matsuoka is a member of SEG, EAGE, SEG Japan and JAPT (Japanese Association for Petroleum Technology). He served as Vice President of SEG from 1997 to 1998 and President of SEG Japan from 2006 to 2008. He received the Best Paper Award from SEG Japan in 1988 and the Japanese Association for Petroleum Technology in 1999.